TERAHERTZ IMAGING WITH SYNTHETIC APERTURE ARRAYS AND ADAPTIVE IMAGE RECONSTRUCTION

by

Zhuopeng Zhang

A thesis submitted to the Faculty of the University of Delaware in partial fulfillment of the requirements for the degree of Master of Science in Electrical and Computer Engineering

Spring 2011

TERAHERTZ IMAGING WITH SYNTHETIC APERTURE ARRAYS AND ADAPTIVE IMAGE RECONSTRUCTION

by
Zhuopeng Zhang

Approved: ______________________________
Takashi Buma, Ph.D.
Professor in charge of thesis on behalf of the Advisory Committee

Approved: ______________________________
Kenneth E. Barner, Ph.D.
Chair of the Department of Electrical and Computer Engineering

Approved: ______________________________
Michael J. Chajes, Ph.D.
Dean of the College of Engineering

Approved: ______________________________
Charles G. Riordan, Ph.D.
Vice Provost for Graduate and Professional Education

ACKNOWLEDGMENTS

I wish to thank my advisor, Takashi Buma, Ph.D., without whom none of this would even have been possible.

I must also thank my parents and grandparents living in China, who are always supporting my pursuit of higher academic degree in USA.

This research was supported by the University of Delaware Research Foundation.

TABLE OF CONTENTS

LIST OF TABLES

LIST OF FIGURES

ABSTRACT

Electromagnetic terahertz (THz) pulses have received considerable interest for imaging applications in security, package inspection, and nondestructive testing[1-4]. Conventional THz imaging systems employ a confocal geometry, where the illumination and detection are focused to the same location. High lateral resolution requires sharply focused THz beams, but this comes at the expense of an extremely short depth of focus. This leads to long acquisition times, which is a major drawback for practical applications. An alternative THz imaging approach uses phased arrays of transmitter and receiver elements[5]. The generation and detection of coherent THz waves allows synthetic aperture techniques from a single transceiver. Image reconstruction involves combining the signals from a collection of transceiver positions. This thesis demonstrates, for the first time to our knowledge, an adaptive reconstruction method for THz imaging. Our approach improves image quality by computing a coherence factor (CF) based on the spatial coherence of the received THz signals. This CF is computed at every image point, where it suppresses undesirable side lobes for improved image contrast. This thesis also describes an adaptive reconstruction for sparse THz arrays. Sparse arrays employ widely separated elements to dramatically reduce array complexity, making them highly attractive for practical applications. However, sparse arrays suffer from grating lobe artifacts[6] that degrade image quality. The key feature of the adaptive technique is to exploit both the spatial and temporal coherence of the single-cycle THz pulses used by the imaging system. Grating lobe artifacts are reduced by 15 dB without any prior knowledge of the object.

Chapter 1

INTRODUCTION AND MOTIVATION

1.1 Terahertz Radiation and its Applications

1.1.1 What is Terahertz Radiation?

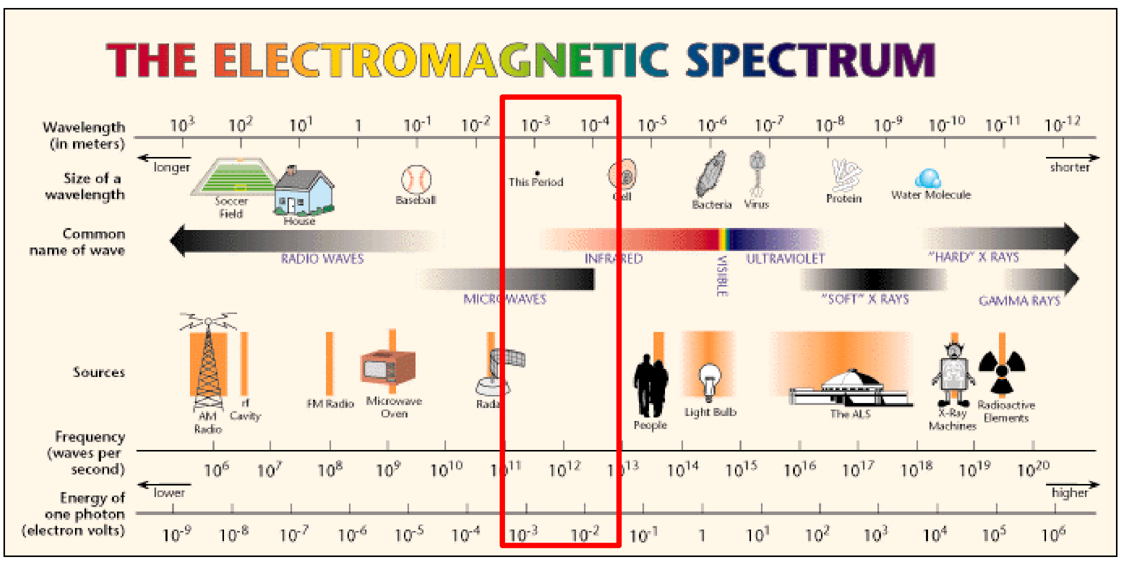

Figure 1.1 **The electromagnetic spectrum. The THz frequency range lies in the middle of this diagram, between "radar" and "people" and is indicated in red. Diagram from the LBL Advanced Light Source website: http://www.lbl.gov/MicroWorlds/ALSTool/EMSpec/EMSpec2.html.**

Terahertz (THz) waves, in physics, refer to electromagnetic radiation in the frequency interval from 0.1 to 10 THz, which is sometime called sub-millimeter waves for the lower frequency bound and far-infrared waves for the higher. The terahertz regime (Fig. 1.1) of the electromagnetic spectrum lies between the mid-infrared and microwave bands, which represents an important transition from wave-like characteristics (microwave) and particle-like characteristics (infrared), or in other word, electronics to photonics.

1.1.2 Characteristics of THz Radiation

Terahertz waves possess several unique features that have been considered as very important to some applications. Listed below are three most interesting advantages:

(a) "Fingerprint" recognition: Many explosives and drugs for security concern have characteristic THz range absorbance lines (Table 1.1), according to which the materials of interest can be thereby identified. Some of these materials are listed in the table below. Lots of other chemical substances also present characteristic absorption features in the THz range, which, in contrast, are almost absent under the lower bound of this 0.3-10 THz gap (in the millimeter and microwave region).

(b) Transmission capability: Most dielectric and non-polar mediums are "transparent" to terahertz radiation. Therefore terahertz waves are able to penetrate the barriers such as plastic, corrugated cardboard, clothing, shoes, ceramics, etc. However out of the higher bound of this 0.3-10 THz gap, say infrared, see these materials as basically opaque.

Table 1.1 Collection of absorbance peak positions of some explosives and drugs[7].

Material	Feature band center position frequency (THz)
Explosive	
Semtex-H	0.72, 1.29, 1.73, 1.88, 2.15, 2.45, 2.57
PE4	0.72, 1.29, 1.73, 1.94, 2.21, 2.48, 2.69
RDX/C4	0.72, 1.26, 1.73
PETN	1.73, 2.01, 2.51
HMX	1.58, 1.84, 1.91, 2.21, 2.57
TNT	1.44, 1.7, 1.91, 5.6, 8.2, 9.1, 9.9
NH_4NO_3	4.7
Drugs	
Methamphetamine	1.2, 1.7-1.8
MDMA	1.4, 1.8
Lactose α-monohydrate	0.54, 1.20, 1.38, 1.82, 2.54, 2.87, 3.29
Icing sugar	1.44, 1.61, 1.82, 2.24, 2.57, 2.84, 3.44
Co-codamol	1.85, 2.09, 2.93
Aspirin, soluble	1.38, 3.26
Aspirin, caplets	1.4, 2.24
Acetaminophen	6.5
Terfenadine	3.2
Naproxen sodium	5.2, 6.5

(c) Bio-harmlessness: Terahertz radiation exposure causes NO health risk to living organism due to its non-ironizing position in the electromagnetic spectrum, which is agreed as another big advantage to X-ray except of "fingerprinting".

The limitation exist in the facts that terahertz waves can cannot penetrate metallic material by (almost complete) reflection and water in both forms of liquid and vapor by absorption (Fig. 1.2).

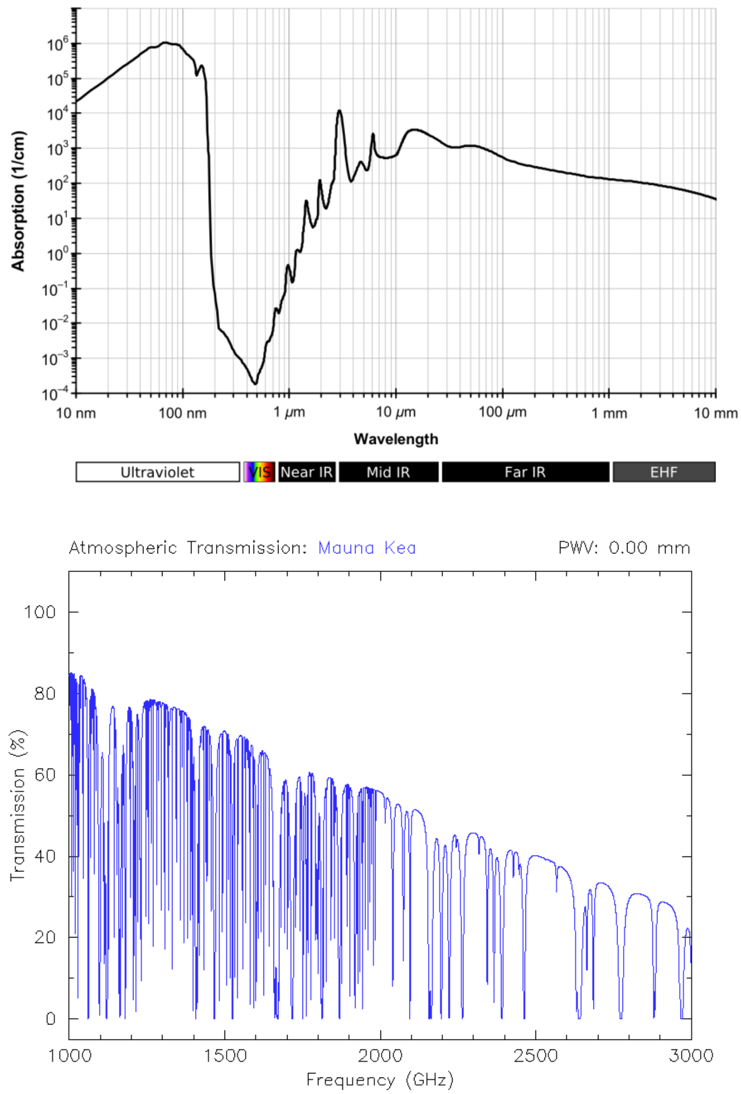

Figure 1.2 Above: liquid water absorption spectrum across a wide wavelength range. Below: Plot of the zenith atmospheric transmission on the summit of Mauna Kea throughout the range of 1 to 3 THz of the electromagnetic spectrum at a precipitable water vapor level of 0.001 mm. (simulated) (source: Wikipedia)

1.1.3 Applications of THz Radiation

Security:

Because transmission capability of terahertz radiation, it can be used for surveillance, such as security screening, to uncover, beneath clothing or packaging, the weapons (Fig. 1.3) by plotting their shape, and identify the explosives or drugs by "fingerprinting" their spectra sensitively, which is a combination of spectroscopy and imaging. By passively detecting a very specific range of materials and objects according to their selected terahertz signatures, privacy related issues can be effectively avoided.

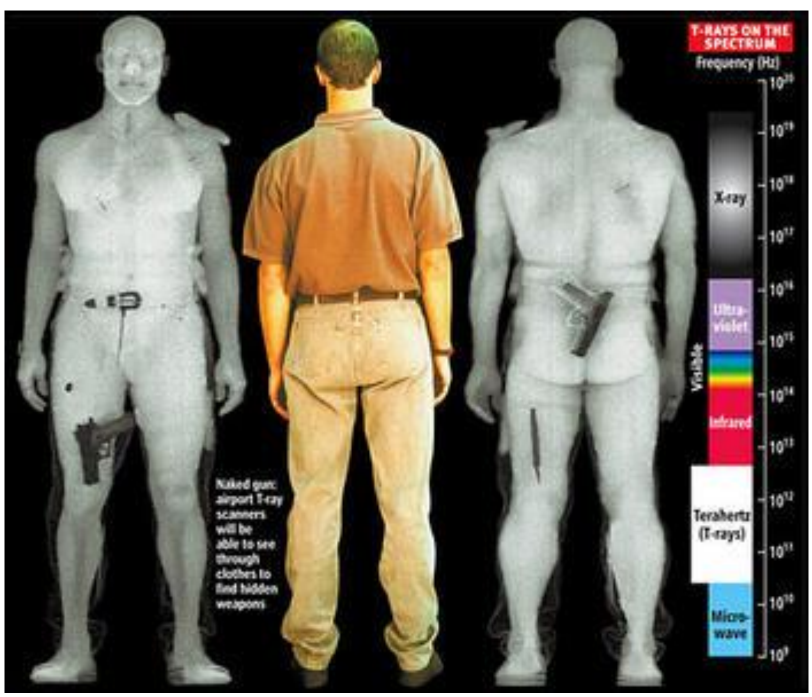

Figure 1.3 Terahertz scanner imagery. (Source: www.dailymail.co.uk)

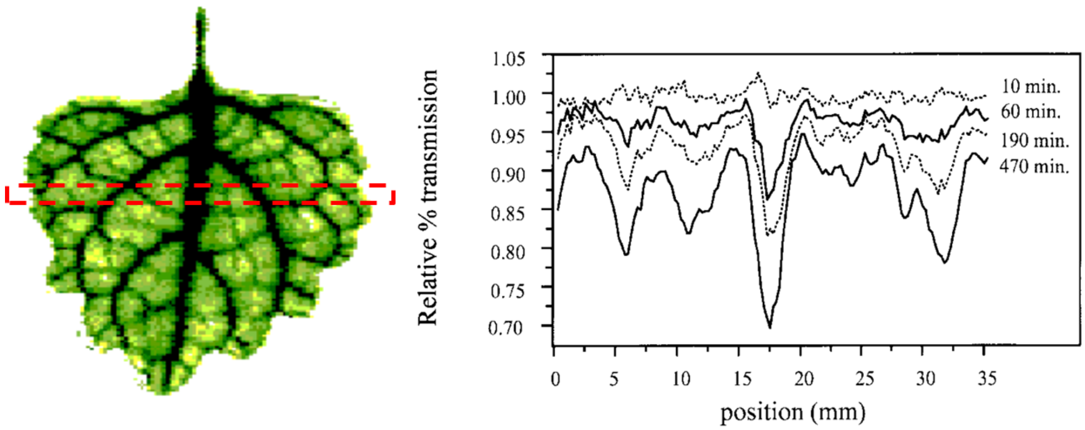

(a) (b)

Figure 1.4 (a) Terahertz image of a leaf from a common houseplant, Coleus[8]. The false color scale is correlated with water content, with darker green indicating more water. The dashed box indicates the approximate position of the line scans of Fig. 1.4 (b) Terahertz line scans along a line that transects the center of the leaf, as shown by the dashed box in (a). The modulation in each line scan results from the stem structure of the leaf. Each scan is labeled according to the time (in minutes) after the plant was watered. Decreasing terahertz transmission results from water intake into the leaf tissue.

Bio-Medical:

Non-ironizing to tissues and DNA in contrast to X-rays allows terahertz radiation the big potential on imaging living body. Terahertz radiation appears to be able to detect certain skin cancers and, possibly, epithelial cancers in the mouth with a safer and less invasive or painful way, due to the facts that some wavelengths of terahertz wave could penetrate several millimeters of tissue with low water content (e.g. fatty tissue) and measure the tissue density according to its absorption amount by water content (Fig. 1.4).

Non-destructive testing:

Terahertz pulses have already been used in NASA to detect the presence of foreign bodies or flaws in outer foam of aerospace shuttle. It is possible to test the structures such as laminates or composites in industry which is somewhat similar to radar detection. On line quality control such as thickness and adhesiveness are also practical with some commercially available product (e.g. T-ray 4000 from Picometrix, LLC).

Other applications:

Other applications include high-altitude telecommunications, near field microscope, semiconductor industry, pharmaceutical industry, and submillimeter astronomy. etc.

1.2 Aim of the Thesis

Among all the applications of terahertz radiation, a lot of them turn out to be an imaging system. Thus it is worthy to investigate into terahertz imaging techniques. And recently, terahertz (THz) pulse has attracted increasing interest for imaging purpose in stand-off security screening, package inspection, nondestructive testing and pharmaceutical tablet coating evaluation.

In a conventional confocal imaging system, the collimated THz beam, after passing through a spherical lens or reflected by an off-axis parabola, focuses to the point-of-interest, where the detection beam is also focused. In a manner of pixel-by-pixel scanning of the focused beam at the area-of-interest, a 2-D image with fine depth resolution can be formed by this single-cycle pulse imaging in time-domain reflection-mode. Finest lateral resolution is obtained given that the beams are strongly focused, which, however, implies the expense of an extremely limited depth of focus. In other word, high-lateral-resolution seeks large numerical aperture while long-focal-depth calls for small one. Thus a 3-D image with good image quality both in lateral and axial requires additional depth-by-depth 2-D scans, leading to the tremendous commitment on time. This is a major drawback for conventional confocal imaging in practical applications.

This thesis demonstrates a virtual-source method to overcome this drawback. The approach employs a synthetic aperture focusing technique (SAFT) combined with temporal coherence weighting to produce images with fine spatial resolution over a large depth range[9]. This virtual-source method can significantly improve the image quality of conventional THz systems for 3-D imaging.

Furthermore, a more aggressive challenge is brought out by sparse arrays employing widely separated elements in order to dramatically reduce array complexity, which is especially important for two-dimensional (2-D) arrays. Unfortunately, highly thinned arrays are plagued by grating lobe artifacts that degrade image quality. The poor image quality of sparse arrays has been a severe limitation for practical applications.

This thesis also demonstrates a sparse array THz imaging technique that significantly reduces grating lobe artifacts without any prior knowledge of the object. The key feature is an adaptive reconstruction algorithm that exploits both the spatial and temporal coherence of the received THz signals.

1.3 Outline of the Thesis

Chapter 2 discusses the method of synthetic aperture focusing technique (SAFT) combining with temporal coherence weighting (CF) factor to address the depth-of-focus issue confronted by conventional confocal imaging. Experimental setup and basic theory are illustrated. Point spread function measurement and enface imaging are subsequently performed. A 3-D imaging is also presented in the end.

Chapter 3 further digs into the sparse array issue and gives out a solution by smartly involving an additional spatial coherence weighting factor, called interference factor (IF), to the technique referred to Chapter 2. Sparse array imaging results (both B-mode and C-mode) are presented as the comparison between the conventional method, method in Chapter 2 and method in Chapter 3.

Chapter 4 concludes the adaptive data reconstruction described in Chapter 2 and 3, and discusses future work.

Chapter 2

ADAPTIVE TERAHERTZ IMAGING (SAFT+CF) FOR EXTENDING DEPTH OF FOCUS

2.1 Overview

As indicated in Chapter1, conventional THz time-domain imaging systems mechanically scan a focused THz beam over the object of interest. Finest spatial resolution requires low f-number (f/#) optics, but this comes at the expense of extremely short depth-of-focus. This in turn requires scanning over all three dimensions of the object, leading to excessively long acquisition times. As an alternative, the depth-of-focus can be extended by using larger f/# optics. However, this reduction in acquisition time comes at the expense of degraded lateral resolution.

Here this thesis introduces a virtual transceiver approach with an adaptive reconstruction algorithm to overcome these limitations. The virtual transceiver is laterally scanned over a single two-dimensional (2-D) region above the object of interest. Signal samples from multiple transceiver positions are combined to produce a synthetic aperture focused at a particular image point[10]. The focusing quality can be significantly improved by using an amplitude weighting factor based on the spatial coherence of the recorded signals[11]. This significantly improves image quality by suppressing undesired sidelobes in a non-iterative self-adaptive manner. To my knowledge, this is the first demonstration of a non-iterative adaptive reconstruction technique for high resolution 3-D THz imaging.

2.2 Basic Theory

2.2.1 Synthetic Aperture Focusing Technique (SAFT)

Fig. 2.1(a) shows the basic imaging geometry, where low f/# optics sharply focus THz waves above the object of interest. The THz focus is treated as both a virtual source and receiver of broadband THz waves. This virtual transceiver is laterally scanned over the object of interest to produce a synthetic array focused at a particular image point, as shown in Fig. 2.1(b). The signal samples $u_m(t)$ from multiple transceiver positions are combined according to[10]:

$$u_{SAFT} = \sum_{m=1}^{M} u_m(\Delta t_m) \qquad (2.1)$$

In Eq. (2.1), Δt_m is the round trip propagation time between a transceiver element and the desired image point. M is the number of elements required to maintain the desired focal ratio for the transceiver aperture. Relatively few transceiver elements are required to reconstruct image points near the array. Image points at larger depths require a larger value of M. When an image point coincides with an actual object, the samples $u_m(\Delta t_m)$ add constructively. Conversely, destructive interference among the samples occurs when an image point is located away from an object.

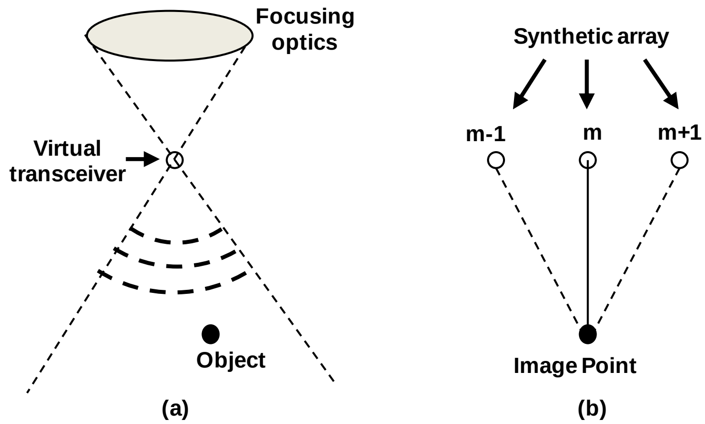

Figure 2.1 **(a) Basic geometry of the virtual transceiver laterally scanned over the object of interest. (b) SAFT involves summing the appropriate signal samples from neighboring elements.**

Simulated data with single-cycle terahertz pulses is shown in Fig. 2.2(a). Each column of the wavefield plot corresponds to the signal from a particular transceiver location. Differences in arrival time of the received echo produce the hyperbola-shaped wavefront. As expected, the earliest arrival time occurs for the center element while the latest arrival times occur for the edge elements. The wavefield plot displays the envelope of the THz signals, which explains the smooth appearance of the received wavefront. The above synthetic aperture focusing technique (SAFT) is a coherent sum, so the signals from all array elements must properly interfere to produce a high quality focus. When an image point coincides with an actual object, the samples um add constructively to produce a large amplitude signal only at the array focus. Likewise, destructive interference among the samples produces a weak signal for an image point located away from the focus. The SAFT reconstruction of the simulated data is shown in Fig. 2.2(b). The cross-sectional image shows a tight focus, indicating fine lateral and depth resolution. The faint wing-shaped features are a normal feature of impulse imaging systems and are often called a “bow-tie” in ultrasound imaging[10]. These are due to the limited aperture of the imaging array, where the signals from edge elements experience incomplete destructive interference.

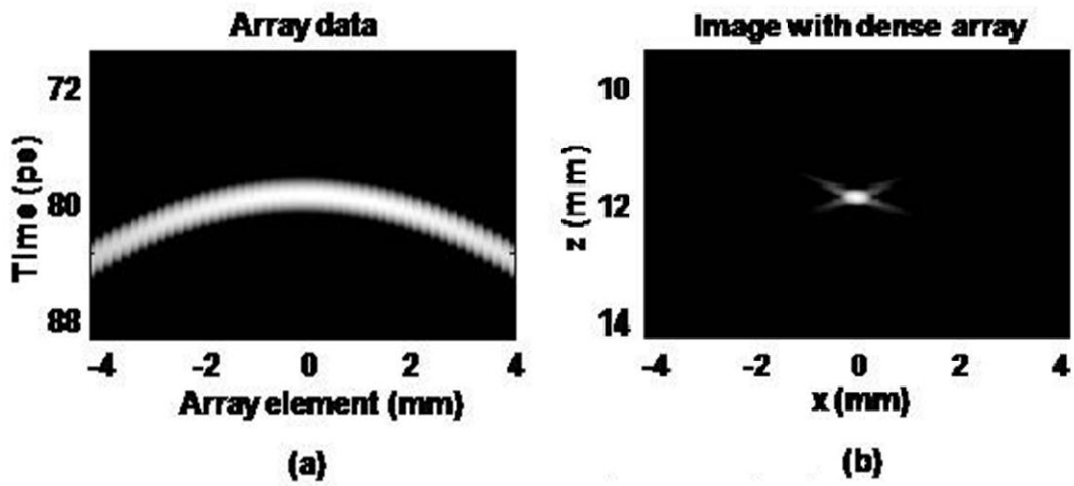

Figure 2.2 **(a) Simulated array data from a point target. (b) Image reconstructed with synthetic aperture focusing technique (SAFT).**

2.2.2 Coherence Weighting (CF)

SAFT processing produces excellent depth-of-focus in THz imaging. Image quality can be further improved in an adaptive manner by exploiting the coherent nature of the THz signals. When an image point coincides with an actual object, the delayed signal samples $u_m(\Delta t_m)$ from each transceiver element are all in-phase to produce constructive interference. This corresponds to high spatial coherence across the transceiver array elements, as shown in Fig. 2(a). When the synthetic focus is steered away from an object, the delayed signal samples are out-of-phase to produce destructive interference. This corresponds to low spatial coherence across the transceiver array, as shown in Fig. 2(b). Low spatial coherence also occurs in image regions containing primarily noise, where the signal phases are randomly aligned (Fig. 2(c)). Therefore, the spatial coherence of the delayed signal samples can serve as a weighting factor to suppress sidelobes and noise. The coherence factor (CF) at a reconstructed image point is defined by[11, 12, 13]:

$$CF = \frac{\left(\sum_{m=1}^{M} u_m(\Delta t_m)\right)^2}{M \sum_{m=1}^{M} u_m(\Delta t_m)^2} \qquad (2.2)$$

In Eq. (2.2), the CF measures the spatial coherence of the delayed signals across the array aperture. The CF is close to unity for image points resulting from high signal coherence. Likewise, image points resulting from low coherence produce a CF close to zero. The final image is obtained by multiplying each image pixel u_{SAFT} with its corresponding CF. This amplitude weighting is self-adaptive in nature since the CF is based entirely on the received data. This combination of SAFT and coherence weighting has been used to improve image quality in ultrasound and photoacoustic imaging[9, 14, 15]. We demonstrate that such adaptive processing can produce high resolution 3-D THz images with large depth-of-focus.

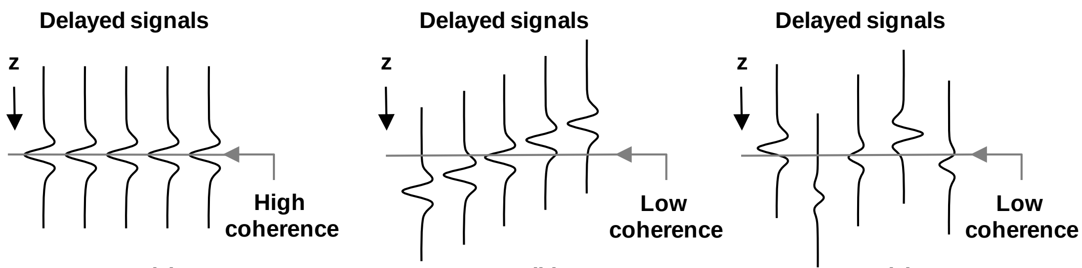

Figure 2.3 (a) High coherence across the transceiver array occurs when the image point coincides with a scattering point within the object. (b) Low coherence occurs when the array is steered away from an actual object point. (c) Low coherence also occurs when the transceiver signals are primarily noise.

2.3 Experimental Setup: a Time-domain Terahertz Imaging System

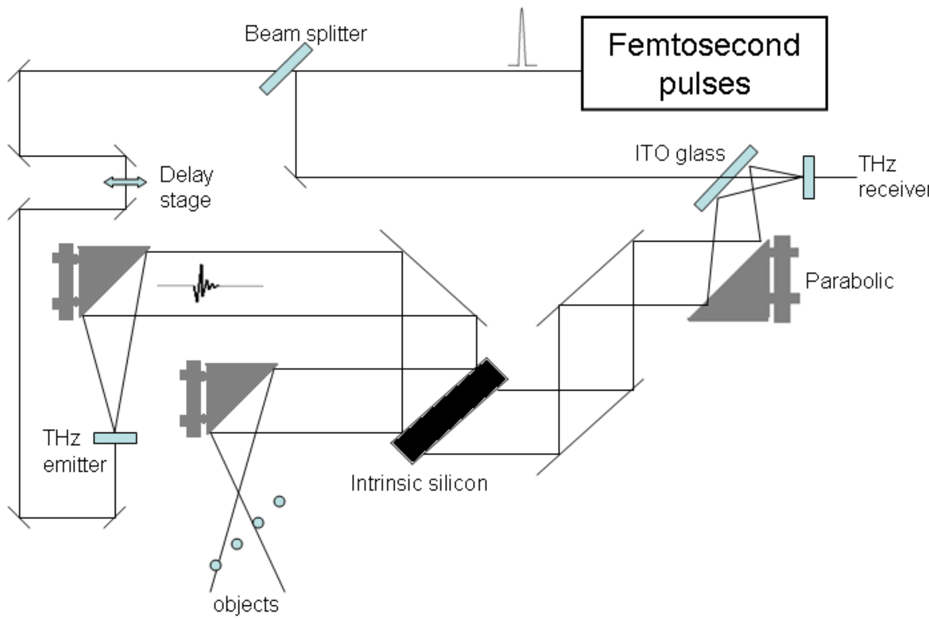

Figure 2.4 Schematic of time-domain THz imaging system.

Imaging experiments are performed with a standard THz time-domain system employing a femtosecond Ti:Sapphire oscillator (KM Labs) emitting sub-30 fs pulses. THz pulses are generated by a photoconductive antenna (Giga Optics) biased with a 60 Vpp square wave at a frequency of 63 kHz. As shown in Fig. 2.4, the emitted THz pulses are collimated with an off-axis parabola and directed to a 6 mm thick high-resistivity silicon beamsplitter. The reflected THz pulses are focused by an f/1 parabola to illuminate the object. The parabola focus serves as both a virtual source and receiver of THz pulses. To simplify the experimental arrangement, a synthetic aperture is produced by laterally scanning the object instead of the transceiver element. Therefore, received THz waves are collected by the f/1 parabola and transmitted through the silicon beamsplitter. A third parabola focuses the THz waves into a 1 mm thick ZnTe crystal for electro-optic detection. An indium tin oxide coated glass slide is used to combine the THz beam with the optical probe pulse. The output from the balanced detector is fed into a lock-in amplifier for phase sensitive detection with respect to the 63 kHz bias voltage of the transmitting antenna. The lock-in amplifier output is then digitized with a 16-bit digitizer (National Instruments) operated by LabVIEW. A rapid scanner (Clark MXR) operating at 2 Hz produces the time delay between the transmit and receive pulses. The sync output from the scanning system serves as the trigger for the digitizer.

2.4 Results

2.4.1 B-mode Imaging

2.4.1.1 Point Spread Function Measurement

The point spread function of the THz imaging system was estimated from cross-sectional images of a 0.8 mm diameter steel wire placed at various depths below the virtual THz transceiver. For each wire depth, the wire is horizontally scanned in 0.10 mm increments over a 10 mm distance. Signals are averaged 64 times before storage. In Fig. 3, the images at different depths are combined to facilitate image display. The wire is parallel to the y-axis in each image (i.e. perpendicular to the image plane). Fig. 2.5(a) shows the result of conventional THz reconstruction, where each image column is obtained from a single scan line. The wire target is in sharp focus at the top of the image, but clearly becomes increasingly out of focus at larger depths. This is the drawback of conventional THz imaging with low f/# optics.

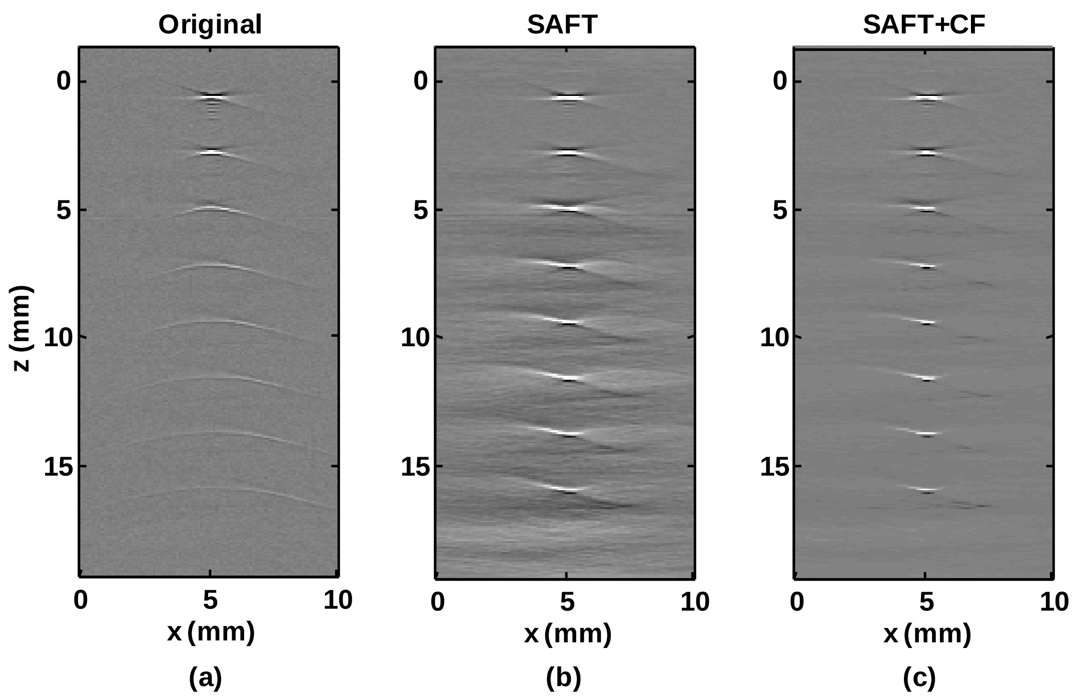

Figure 2.5 Wire target images using (a) conventional processing (b) SAFT processing (c) SAFT+CF processing. The most significant improvement in image quality occurs at large image depths.

SAFT processing of this same data produces the result in Fig. 2.5(b). SAFT refocuses signals to maintain fine spatial resolution at larger depths. For any given depth, the proper number of elements was chosen to maintain a f/2 synthetic aperture. The signal values involved in SAFT processing are also used to compute the CF at each image point. The resulting CF map is multiplied with the SAFT image to produce the final image in Fig. 2.5(c). Clearly, a much cleaner image is produced when SAFT and coherence weighting are used together. SAFT typically produces a point spread function with strong sidelobes[10], which appear as the “wing-like” features surrounding each wire target in Fig. 2.5(b). Coherence weighting suppresses these sidelobes to significantly improve image quality. At larger depths, a faint artifact is located to the right of each wire target (near x = 7 mm). These are due to stray reflections from the sample holder and are not a result of SAFT+CF processing. The illuminating THz beam diameter increases with target depth, leading to stronger stray reflections. Digitally removing the spurious signals from the recorded THz data produces an artifact-free image (not shown in Fig.2.5), supporting the above hypothesis. The slightly asymmetric appearance of the wire target images in Fig. 3(b) and (c) is due to a small misalignment in the THz focusing optics. Analyzing the wire target signals of Fig. 3(a) reveals the THz beam propagates at an 11 degree angle with respect to the z-axis. Through performing imaging simulations accounting for such an angular deviation, the slightly asymmetric appearance of the wire targets could successfully be reproduced.

2.4.1.2 Signal-to-noise Ratio

Improved signal-to-noise ratio (SNR) is evident in the SAFT image of Fig. 2.5(b). The SNR improvement is a natural result of the synthetic aperture process, where signal summation essentially acts as a form of signal averaging. Coherence weighting further improves SNR in an adaptive manner. As shown in Eq. (2.2), the numerator of the CF is essentially a coherent sum while the denominator is an incoherent sum. Image regions containing primarily noise will therefore produce a low CF value. In one sense, the noise suppresses itself in the final image. By contrast, image regions corresponding to actual objects are preserved by coherence weighting. This adaptive noise suppression leads to enhanced SNR in the image of Fig. 2.5(c).

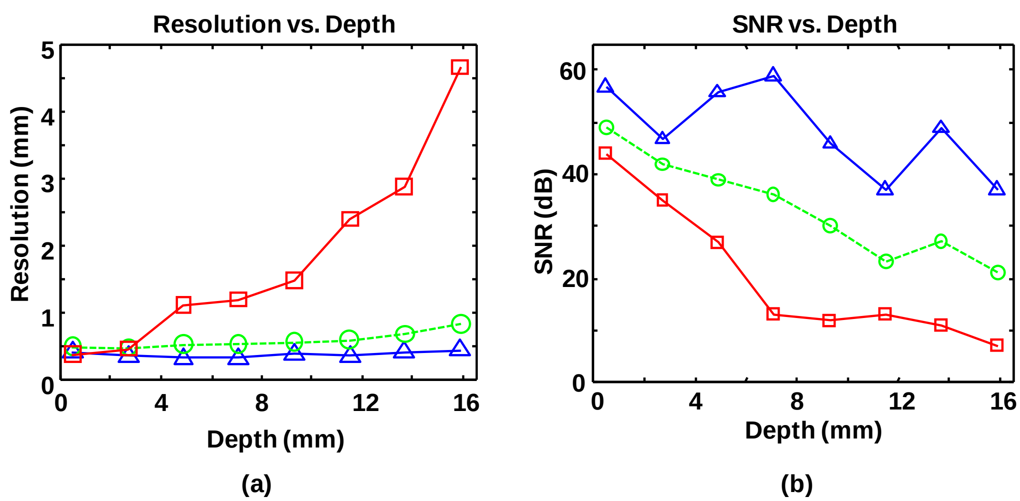

Figure 2.6 Image quality comparison between no processing (squares), SAFT (circles), and SAFT+CF (triangles). (a) Lateral resolution as a function of depth. (b) SNR as a function of depth.

Quantitative comparisons of lateral resolution and SNR are shown in Fig. 2.6(a) and (b), respectively. At a particular target depth, resolution is defined as the -6 dB width of the wire image. SNR is defined as the ratio of the average signal intensity in the brightest portion of the wire image to the average noise intensity at the same depth. In conventional processing, resolution degrades by an order of magnitude over the 16 mm range of target depths. This is accompanied by extremely poor SNR at large depths. The refocusing effect of SAFT processing significantly improves both lateral resolution and SNR. At the largest target depth, the SAFT image exhibits a five-fold improvement in resolution and a 14 dB improvement in SNR compared to conventional processing. Additional improvement is obtained with coherence weighting, resulting in a nearly depth-independent spatial resolution of 0.4 mm. At the largest target depth, the SNR is 30 dB higher than conventional THz imaging (i.e. no processing).

2.4.2 C-mode Imaging

2.4.2.1 Two-dimensional En-face Imaging:

Images of the U.S. Air Force resolution target using conventional and SAFT + CF reconstruction algorithms are shown in Fig. 2.7(c) and (d), respectively. The 0.5 mm wide bar patterns are poorly resolved in the conventional image at depth of 6mm but visualized very well with the SAFT + CF image. The image quality even looks to be better than conventional image at focal plane. Quantitative view could be seen in Fig 2.8.

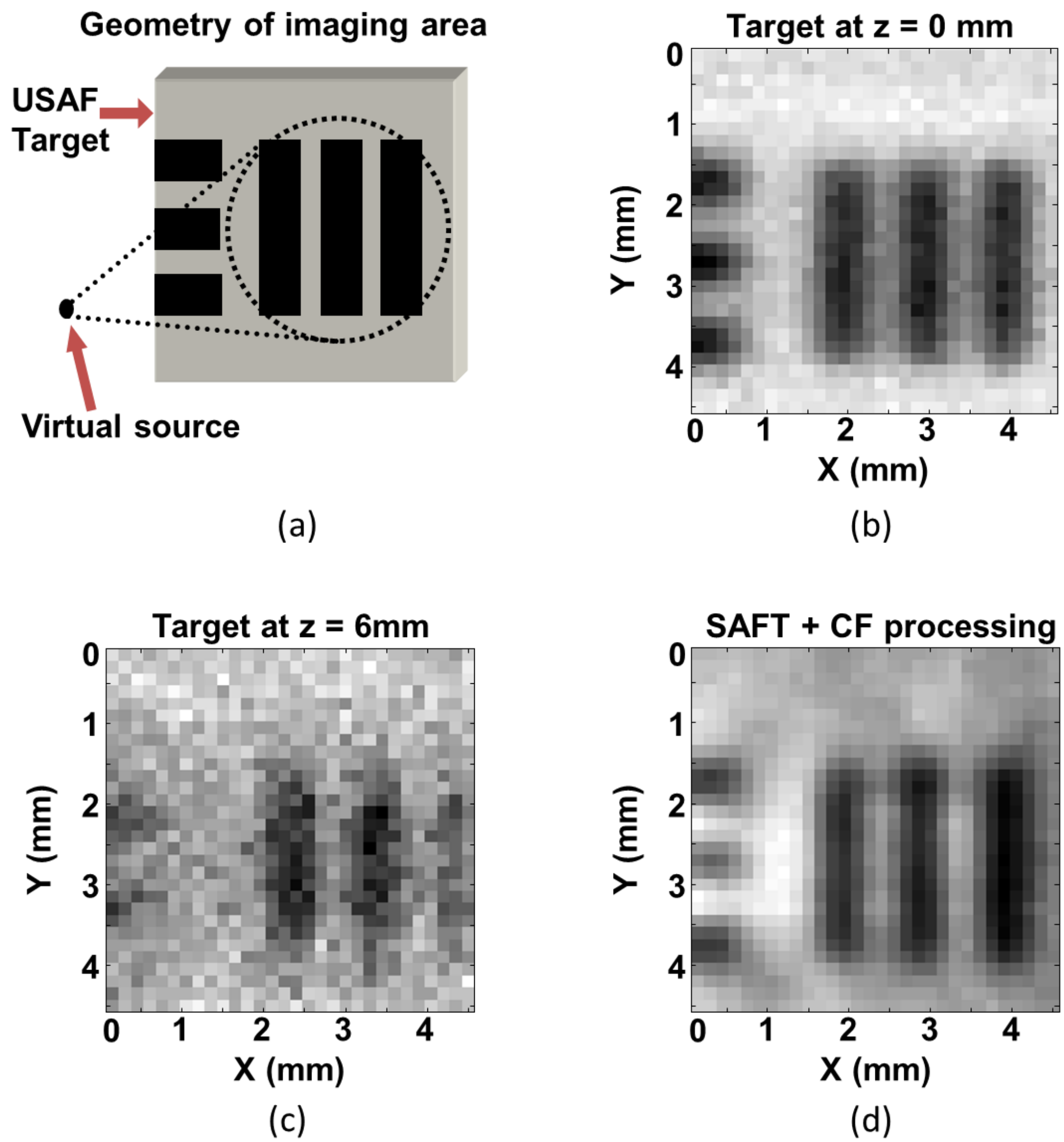

Figure 2.7 (a) Geometry for imaging a USAF resolution target (b) Image from conventional reconstruction algorithm at focal plane, and (c) 6mm below the focal plane. (d) Same data processed with SAFT + CF weighting, showing significantly improved resolution and SNR.

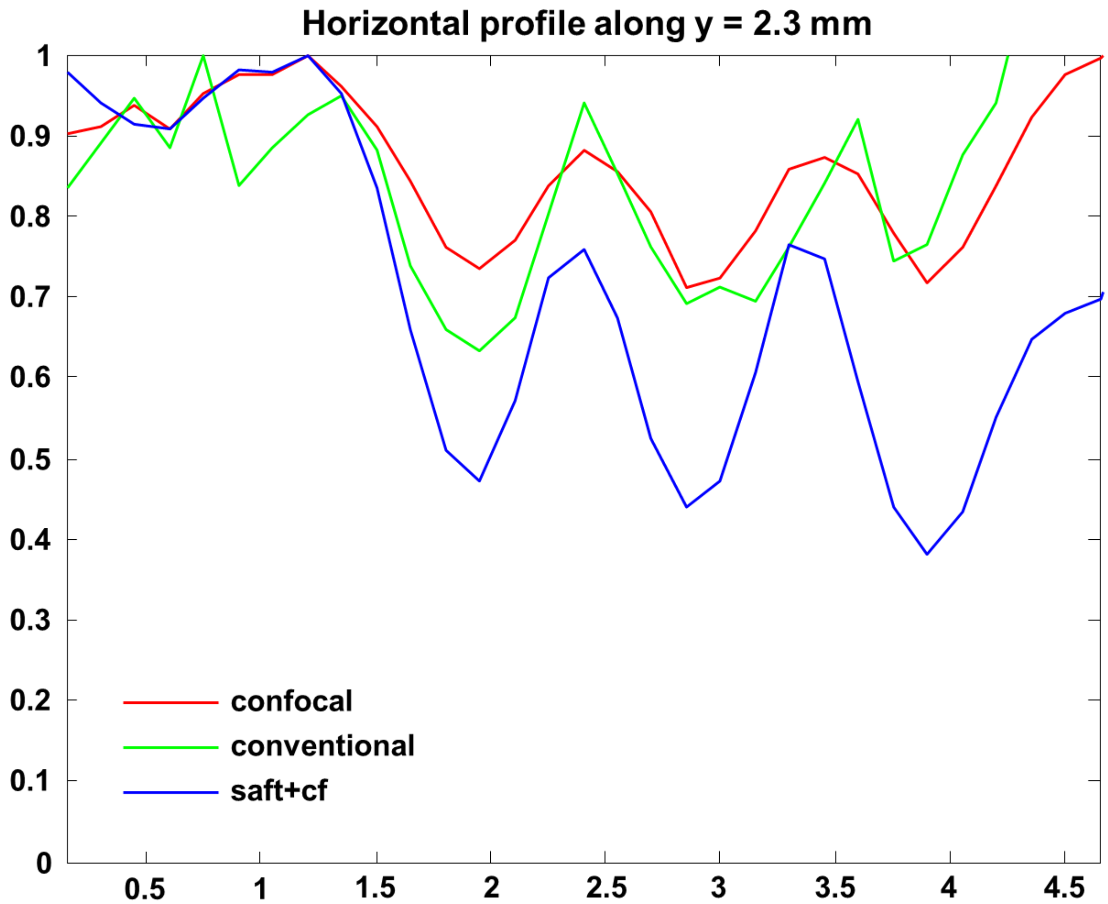

Figure 2.8 **Horizontal plots along the center of images in Fig. 2.7. Red line is for 2.7(b), green line for 2.7(c), and blue line for 2.7(d).**

2.4.2.2 High Resolution 3-D THz Imaging:

High resolution 3-D imaging is achieved with SAFT+CF processing. A 21 gauge needle was placed 9 mm in front of a metal razor blade (Fig 2.9). This 3-D object was laterally scanned over a 50 x 50 pixel grid in 0.2 mm increments. The THz transceiver depth coincides with the front side of the needle. Fig. 2.10(a) shows separate en face images of the needle and razor blade without processing. The dynamic range is adjusted in order to visualize the noisy and blurred image of the razor blade. Fig. 2.10(b) shows the result of SAFT+CF processing. The razor blade is clearly reconstructed with significantly improved resolution and SNR. A stack of SAFT+CF images within a 10 x 10 x 10 mm volume are displayed in the 3-D rendered image in Fig. 2.10(c). It is worth emphasizing that 3-D image reconstruction only requires the virtual transceiver to be scanned over a single 2-D grid of positions. The ability to resolve the tapered tip of the hollow needle (less than 0.8 mm thick) demonstrates the fine depth resolution of THz time-domain imaging. Therefore, more complicated 3-D objects can be reconstructed accurately with the excellent lateral and depth resolution of our adaptive THz imaging approach.

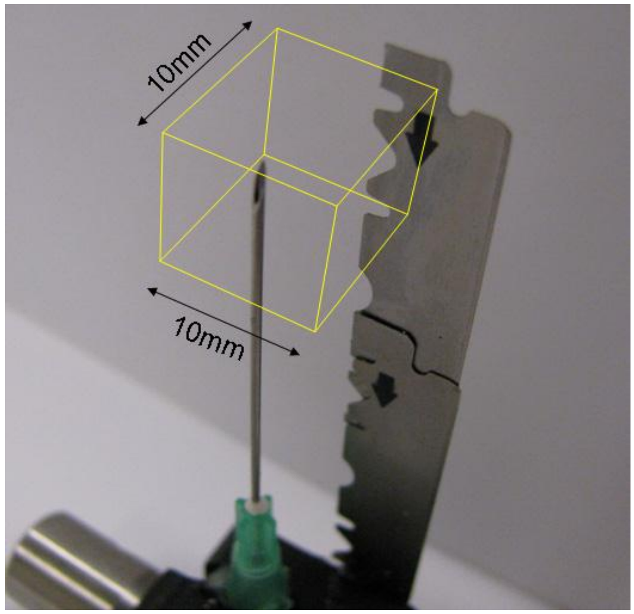

Figure 2.9 The three dimensional object is composed by A 21 gauge needle was placed 9 mm in front of a metal razor blade. This 3-D object was laterally scanned over a 50 x 50 pixel grid in 0.2 mm increments.

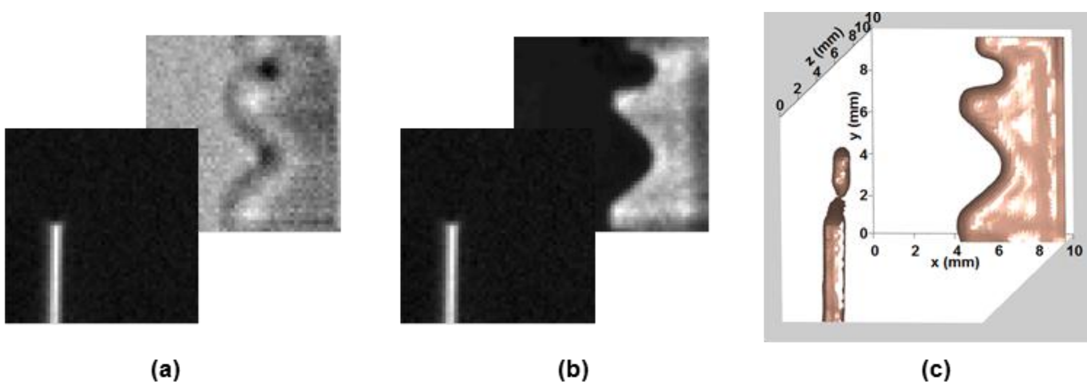

Figure 2.10 Separate en face images of the front needle surface and razor blade (a) without processing and (b) with SAFT+CF processing. (c) Three-dimensional stack of SAFT+CF en face images within a 10 x 10 x 10 mm volume.

Chapter 3

IMPROVED ADAPTIVE IMAGING (SAFT+CF+IF) FOR SPARSE ARRAY

3.1 Overview

Since time-domain THz systems employ single-cycle pulses, the mean wavelength of the THz power spectrum provides a useful length scale for the array geometr[5]. Assuming a mean frequency of 1 THz, a proper phased array for THz impulse imaging requires an element spacing of 0.15 mm. Such densely populated arrays are extremely time consuming to synthesize over a large area, leading to extremely long acquisition times.

Sparse arrays employ widely separated elements to dramatically reduce array complexity, making them highly attractive for practical applications. Unfortunately, sparse arrays are plagued by grating lobe artifacts that degrade image quality[16]. In narrowband sparse arrays, grating lobes occur when the THz propagation path difference between neighboring elements is an integer multiple of a wavelength. The undesired constructive interference produces large amplitude artifacts in the reconstructed image. Grating lobe artifacts occur in a different form in ultrawideband sparse arrays. Propagation path differences exceeding a single-cycle result in complete walk-off between signals from neighboring elements. The non-interfering pulses appear as ripple-shaped artifacts in the reconstructed image[17]. The poor image quality of sparse arrays has been a severe limitation for practical applications.

The majority of efforts to improve sparse array image quality have involved optimizing the spatial distribution of the array elements in transmit, receive, or both[17]. Other approaches interpolate the received data to emulate a fully populated array[18]. In narrowband sparse arrays, a quasi-random distribution of elements significantly reduces the strength of the grating lobes compared to a periodic arrangement of elements. However, the situation is considerably different for an ultrawideband array, where a periodic distribution performs better[17]. Grating lobe levels can be further reduced by array apodization, where amplitude weights are applied to individual array elements[19]. The apodization coefficients are determined in advance (i.e. a lookup table), without any regard to the object of interest. We demonstrate a sparse array THz imaging technique that significantly reduces grating lobe artifacts in an adaptive manner. In other words, the data itself is used to improve the image. The key feature of our adaptive reconstruction algorithm is to exploit the spatial and temporal coherence of single-cycle THz pulses.

3.2 Basic Theory

3.2.1 Grating Lobes

For closely spaced array elements, the array behaves as if it were a continuous aperture to produce a well behaved point spread function. “Close spacing” means the element spacing must be less than half a wavelength for narrowband arrays. For THz impulse imaging systems employing single-cycle pulses, the appropriate “wavelength” is approximately the mean wavelength of the power spectrum. For example, if an array uses single-cycle pulses with a mean frequency of 1 THz, proper synthetic aperture focusing requires the element spacing to be less than 0.15 mm.

If the element spacing is too large, undesired large amplitude signals can occur away from the desired beam direction and focal point. This undesired constructive interference occurs when the THz propagation path difference between neighboring elements is an integer multiple of a wavelength. These are called grating lobes for narrowband arrays, in analogy to the multiple orders of a diffraction grating. Grating lobes are undesirable because they produce severe image artifacts (i.e. ghost images). Grating lobe artifacts occur in a different form in ultrawideband sparse arrays. Propagation path differences exceeding a single-cycle result in complete walk-off between signals from neighboring elements. The non-interfering pulses appear as ripple-shaped artifacts in the reconstructed image.

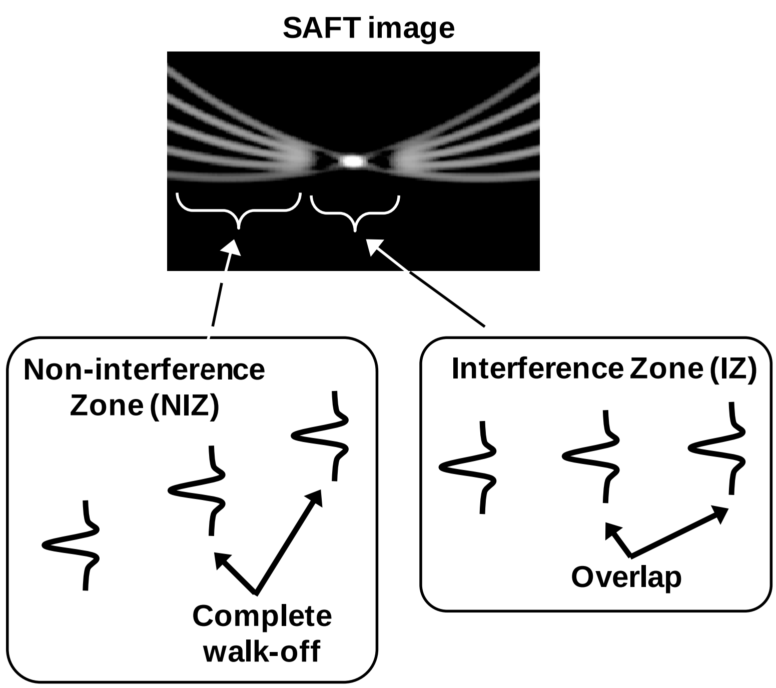

Figure 3.1 Proper image reconstruction occurs within the interference zone (IZ), where individual signals overlap. Grating lobes occur in the non-interference zone (NIZ), where pulse walk-off occurs between neighboring signals.

As an example, a simulated THz impulse image of a point target image with a sparse array is shown in Fig. 3.1, where the immediate vicinity of the point target is fairly well reconstructed by the sparse array. The good image quality in this region is due to proper interference between signals from nearest-neighbor elements. Therefore, SAFT performs well inside this “interference zone” (IZ) [17]. Grating lobes exist outside the IZ, where pulse walk-off occurs between nearest-neighbor signals. Therefore, this “non-interference zone” (NIZ) is responsible for poor image quality. Our basic hypothesis is that the NIZ in the reconstructed image can be suppressed by adaptively monitoring the degree of interference between nearest-neighbor signals.

3.2.2 Interference Factor (IF)

Our adaptive reconstruction algorithm reduces grating lobe artifacts by introducing two amplitude weighting coefficients to the SAFT reconstruction described by Eq. (2.1). These coefficients are based on the data, without any prior knowledge of the object. The first adaptive coefficient is an “interference factor” (IF) that essentially performs cross-correlation analysis to measure the degree of walk-off between time-delayed signals of neighboring elements. The IF is close to unity inside the IZ, but is close to zero in the NIZ. Every image point requires an IF to be computed for each array element. The IF coefficients involve cross-correlating signal samples used to reconstruct image points over a depth range from $p(x,y,z\text{-}\Delta L/2)$ to $p(x,y,z+\Delta L/2)$. For the sake of simplicity, the IF computation will be described for a 1-D sparse array. As sketched in Fig. 3.2(a), the signal u_m from the element at position x_m is cross-correlated with the signals u_{m-1} and u_{m+1} from its nearest neighbors using:

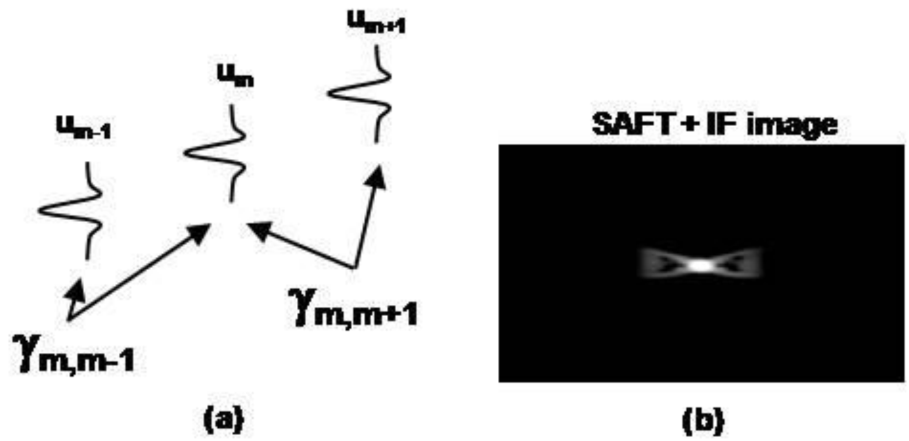

Figure 3.2 (a) The interference factor involves cross-correlating the signal um with its nearest-neighbor signals um-1 and um+1. (b) Image reconstruction with SAFT + IF significantly suppresses grating lobes.

$$\gamma(x_m, x_{m-1}; k) = \frac{2\sum_{n=0}^{N-1} u_m^*[n]\, u_{m-1}[n+k]}{\sum_{n=0}^{N-1}\left(|u_m[n]|^2 + |u_{m-1}[n]|^2 \right)} \qquad (3.1a)$$

$$\gamma(x_m, x_{m+1}; k) = \frac{2\sum_{n=0}^{N-1} u_m^*[n]\, u_{m+1}[n+k]}{\sum_{n=0}^{N-1}\left(|u_m[n]|^2 + |u_{m+1}[n]|^2 \right)} \qquad (3.1b)$$

The correlation window spans from z-$\Delta L/2$ (n=0) to z+$\Delta L/2$ (n=N). The correlation window length N must be long enough to adequately detect pulse walk-off between nearest-neighbor signals, but short enough to maintain decent depth contrast. The IF_m is then computed by the normalized cross-correlation at zero lag between γ (xm,xm-1;k) and γ (xm,xm+1;k):

$$IF_m = \frac{2\left|\sum_{k=-N/2}^{(N/2)-1} \gamma^*(x_m, x_{m-1}; k)\gamma(x_m, x_{m+1}; k)\right|}{\sum_{k=-N/2}^{(N/2)-1}\left(\left|\gamma(x_m, x_{m-1}; k)\right|^2 + \left|\gamma(x_m, x_{m+1}; k)\right|^2\right)} \qquad (3.2)$$

It is worth noting that Eq. (3.1) resembles the expression for fringe visibility in a Young's double slit interference experiment[20]. In this context, Eq. (3.1) computes the fringe visibility over all portions of the interference pattern between nearest-neighbor signals. Eq. (3.2) then computes the degree of overlap between the two fringe visibility patterns.

The modified reconstruction formula is now given by:

$$p(\mathbf{r}) = \sum_{m=1}^{M} IF_m u_m\left(\tau(\mathbf{r}, \mathbf{r}_m)\right) \qquad (3.3)$$

Fig. 3.2(b) shows the image using reconstruction with Eq. (3.3). The grating lobe artifacts are greatly suppressed in the SAFT+IF image, while the immediate vicinity of the point object is virtually unaffected. This demonstrates that the IF successfully preserves the IZ while suppressing the NIZ portions of the sparse array image. However, the image in Fig. 3.2(b) is still inferior to that of Fig. 2.2(b).

Although the SAFT+IF approach significantly suppresses grating lobes, the sidelobes of the point spread function are still fairly high. This is shown by the more pronounced wings surrounding the point object in Fig. 3.2(b) compared to those in Fig. 2.2(b). We therefore reapply the CF introduced in Chapter 2 to suppress the sidelobes.

For each image point, the IF and CF values are computed and applied to the time-delayed signals during coherent summation. Therefore, the "adaptively corrected" synthetic aperture focusing equation is given by:

$$p(\mathbf{r}) = CF(\mathbf{r}) \sum_{m=1}^{M} IF_m u_m\left(\tau(\mathbf{r}, \mathbf{r}_m)\right) \qquad (3.4)$$

Fig. 3.3 shows the image using adaptive reconstruction with Eq. (3.4). Both the grating lobes and sidelobes of the image are greatly suppressed, leading to a high quality focus.

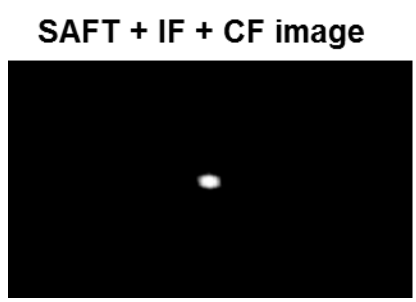

Figure 3.3 Adaptive image reconstruction with SAFT + IF + CF produces a high quality focus.

3.3 Results

3.3.1 1-D Sparse Array Results

Cross-sectional imaging along the x-z plane was performed with a one-dimensional (1-D) sparse array located at z = 0. The array consists of nine elements located at x = [-4d, -3d, …, 3d, 4d], where d = 1.36 mm. This corresponds to an inter-element spacing slightly greater than 4λ at 1 THz. A wire target was placed along the z-axis at z = 10, 12, and 14 mm. The target was imaged at each depth in separate scans, but the recorded data was combined to simplify image display. In general, reconstructing a particular image point (x,z) does not involve all array elements. During reconstruction, the number of elements is adjusted to maintain an f/1.5 aperture. Image depths at z = 10, 12, and 14 mm are reconstructed with five, six, and seven elements, respectively. These elements contribute equally in conventional SAFT reconstruction. In adaptive reconstruction, the contribution of each element is scaled by the interference factor. All B-mode images cover a 6 x 10 mm region and are displayed over a linear gray scale.

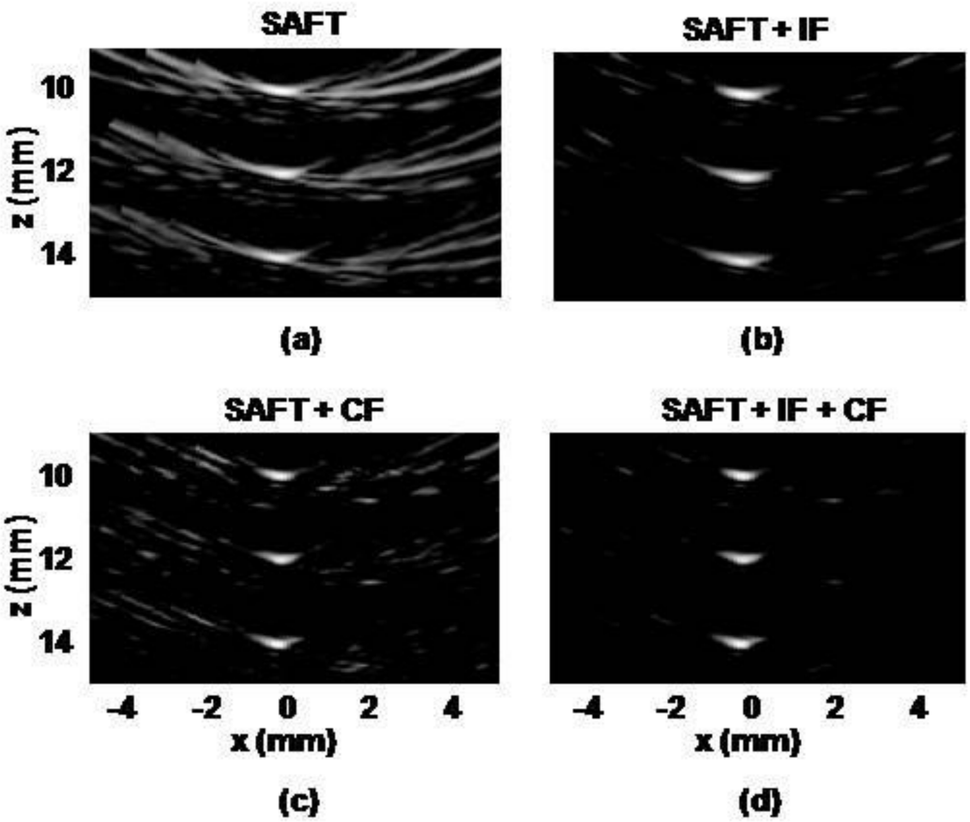

Figure 3.4 **Cross-sectional images reconstructed with (a) SAFT only, (b) SAFT+IF, (c) SAFT+CF, (d) SAFT+IF+CF. All images shown over a 20 dB logarithmic scale.**

Fig. 3.4(a) shows the B-mode images using conventional SAFT using Eq. (2.1). Clearly, the image shows severe grating lobes. Reconstruction using only the CF or only the IF during coherent summation is shown in Fig. 3.4(b) and 3.4(c), respectively. The grating lobes are reduced for both images. The IF outperforms the CF in regions far away from the point target, which is where significant pulse walk-off occurs between neighboring signals. Both the CF and IF are used in Fig. 3.4(d), where the grating lobes are reduced even further to produce the greatest improvement in image quality.

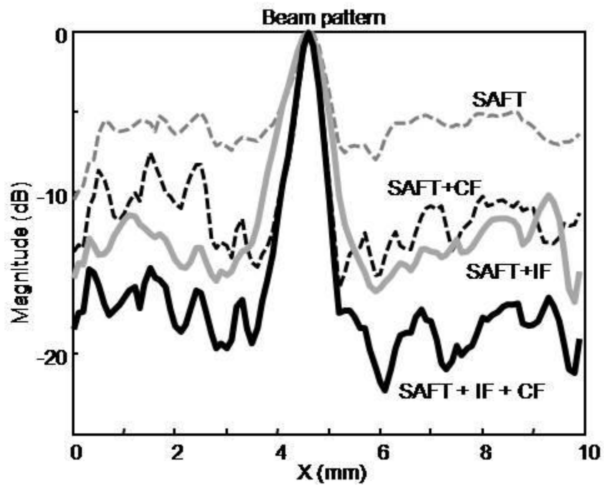

Figure 3.5 Beam patterns for the image of the point target at z = 12 mm using SAFT (dashed gray), SAFT+CF (dashed black), SAFT+IF (solid gray), and SAFT+IF+CF (solid black).

A more quantitative analysis of the grating lobe reduction is achieved by displaying the energy contained in each column of the cross-sectional image for a particular wire target. The resulting beam pattern for the wire target at z = 12 mm is shown in Fig. 3.5. The SAFT image grating lobes produce a broad background approximately -5 dB lower than the main lobe. The IF and CF each reduce the background level. However, combining the IF and CF produces the largest improvement, where the background is -17 dB lower than the main lobe. This improvement is impressive, considering that only six elements are used in the adaptive reconstruction.

3.3.2 2-D Sparse Array Results

En face imaging was performed on two razor blades, one located at z=12 mm and the other at z=12.6 mm. A 56 56 element sparse array was synthesized with an element spacing of 1.36 mm. Figure 3.6(a) shows the SAFT reconstruction at z=12 mm. Each image point used only a subset of array elements to maintain an f /2 imaging aperture. The right-hand half of the image correctly shows the razor blade at z=12 mm, but the left-hand half exhibits strong artifacts from the out-of-plane blade at z =12.6 mm. Strong artifacts exist even in the SAFT +CF image, as shown in Fig. 3.6(b). The fully adaptive reconstruction is shown in Fig. 3.6(c), where the artifact is highly suppressed. The IF for a 2D sparse array element involves cross-correlations with four nearest-neighbor elements. The IF is then computed with a normalized fourth-order correlation at zero lag. For comparison, Fig. 3.6(d) displays a time slice of the raw data at z=12 mm. This unprocessed image has a poor signal-to-noise ratio, since the diverging THz beam is about 6 mm wide at z=12 mm. As expected, the blade edges are blurred, but the time gating displays the central gap of the blade surprisingly well. Plots of the middle row in each image are shown in Fig. 3.7. Clearly, the IF is primarily responsible for suppressing grating lobe artifacts. Reconstruction artifacts are suppressed by over 30 dB, resulting in a clean image. In comparison, the profile of the unprocessed image exhibits a noisy background that degrades image quality.

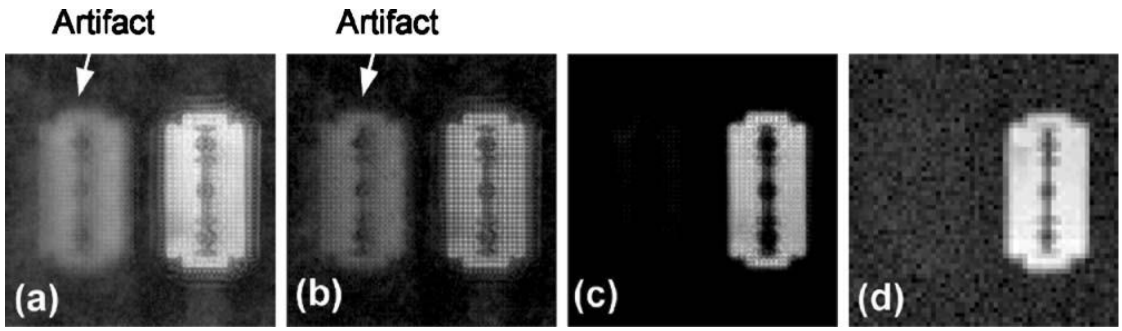

Figure 3.6 En face images reconstructed with (a) SAFT, (b) SAFT+CF, (c) SAFT+CF+IF, (d) no processing. All images have a 40 dB scale (72*72 mm area).

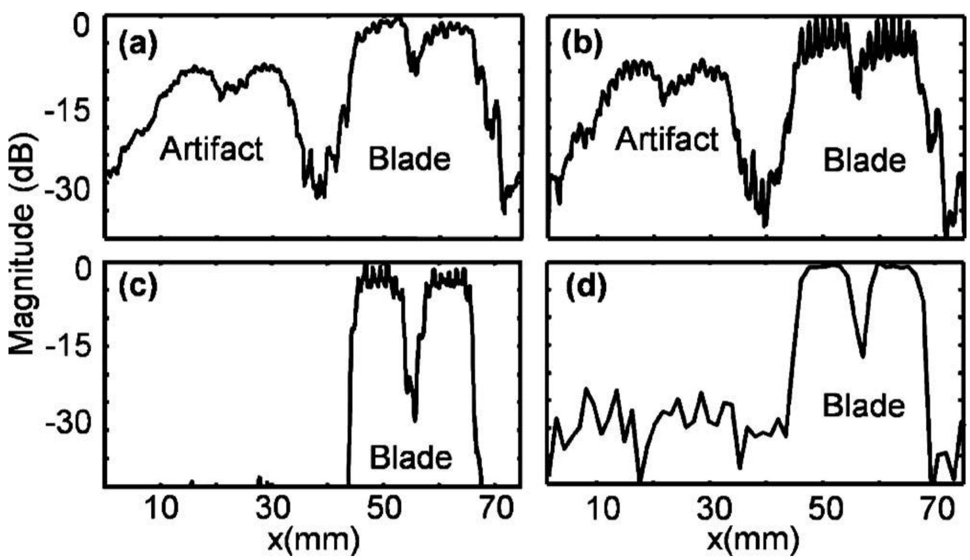

Figure 3.7 Central row of images formed with (a) SAFT, (b) SAFT+CF, (c) SAFT+CF+IF, (d) no processing.

Fig. 3.8 shows C-mode images at z = 12.6 mm. Conventional reconstruction does not show significant grating lobe artifacts, as shown in Fig. 3.8(a). Grating lobe artifacts generally occur at z-planes above the actual object. This is most clearly shown in the simulated B-mode image in Fig. 3.1, where the ripple-shaped artifacts mostly reside above the actual point-object. Therefore, it is not surprising that the razor blade at z = 12 mm does not produce grating lobe artifacts at z = 12.6 mm. Although conventional reconstruction does not produce severe grating lobe artifacts, overall image contrast is significantly improved with SAFT+CF+IF adaptive reconstruction, as shown in Fig. 3.8(b).

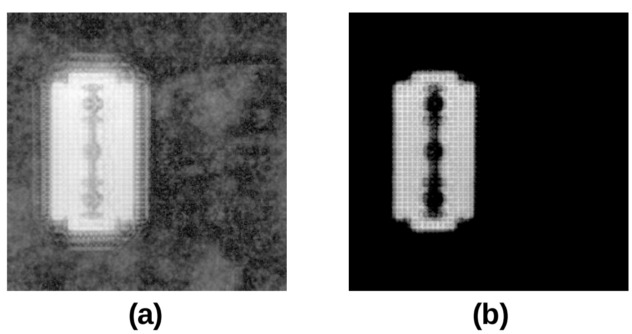

Figure 3.8 C-mode images of the razor blade at z = 12.6 mm using (a) conventional, (b) adaptive reconstruction.

3.4 Discussion: IF vs. CF

Further analysis of the experimental en-face images confirms that the interference factor (IF) is primarily responsible for suppressing grating lobe artifacts. Fig. 3.9(a) shows a plot of the middle row in the C-mode image at z = 12 mm, where Eq. (3.4) is used for reconstruction. The grating lobe suppression is actually better when only SAFT+IF is used, in comparison to the SAFT+IF+CF plot shown in Fig. 3.4(d). We have found that the CF further improves image quality for point-like objects and diffusely scattering bodies, but introduces slight artifacts for specular reflecting objects such as a razor blade. These are particularly apparent in the lower plot of Fig. 3.9(a), which corresponds to an image reconstructed with SAFT+CF. It is clear that the CF is not nearly as effective as the IF in suppressing grating lobes. Furthermore, the profile of the razor blade clearly shows enhanced comb-like “teeth”. Fig. 3.9(b) depicts a possible physical explanation of these artifacts. The intersections of the widely separated wavefronts are regions of high spatial coherence, which are preferentially weighted by the CF. Methods to modify the CF to account for these “false positive” regions of strong spatial coherence are currently under investigation.

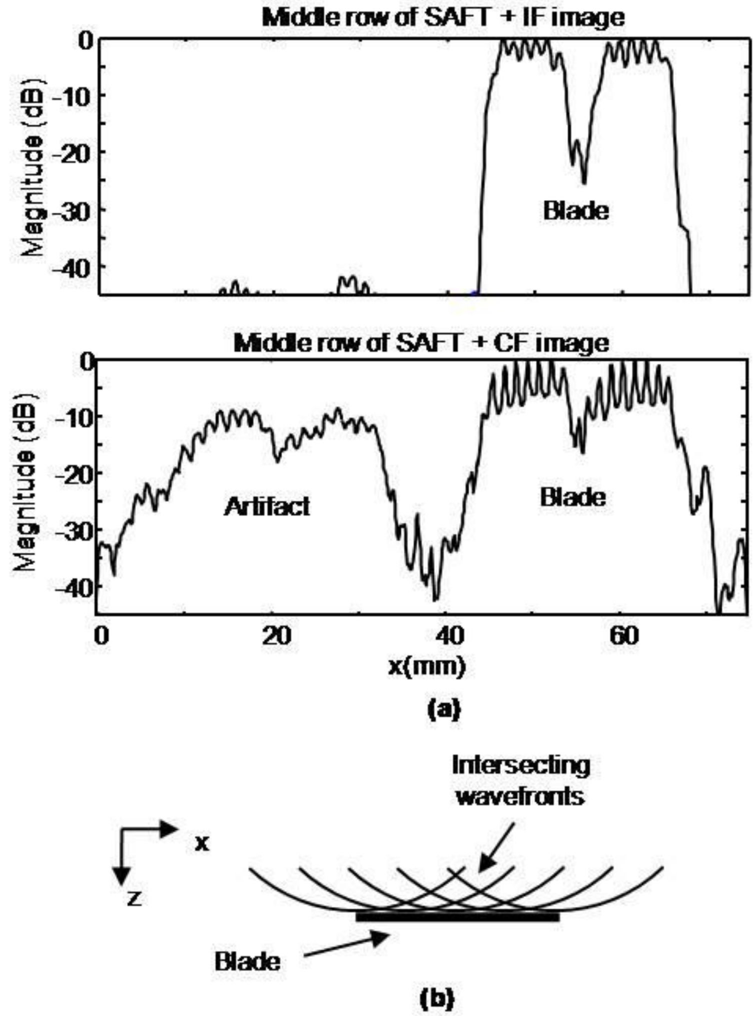

Figure 3.9 (a) Profiles of the middle row of the en-face image at z = 12 mm using SAFT+IF and SAFT+CF reconstruction. (b) Sketch depicting the origin of the slightly jagged appearance of the razor blade.

The IF has negligible effect on lateral resolution, which is measured by the main lobe width of the point spread function. The main lobe lies within the "interference zone" (IZ), where proper interference occurs between signals from nearest-neighbor elements. Since the IF is near unity throughout this zone, the main lobe remains largely unaffected. This is supported by the simulated point object reconstruction in Fig. 3.2(b). This is further supported by the beam patterns in Fig. 3.5, where the main lobes are very similar for SAFT-only and SAFT+IF reconstruction. However, Fig. 3.5 also shows that lateral resolution is somewhat improved by the coherence factor (CF). This has also been observed with a fully populated 1-D THz array employing SAFT+CF [21]. The peak of the array focus corresponds to zero phase difference across the entire array aperture. The phase difference increases for image points further away from the array focus. This destructive interference results in a finite width of the point spread function. In one sense, the CF enhances this destructive interference to produce a slightly narrower array focus and therefore improved spatial resolution. Furthermore, the CF also lowers the sidelobes of the array focus, which improves overall image contrast. Adaptive reconstruction with both the IF and CF produces the most significant improvement in overall image quality.

Chapter 4

SUMMARY AND FUTURE WORK

This thesis has demonstrated sparse terahertz arrays with significantly improved image quality using a non-iterative adaptive reconstruction technique. The temporal and spatial coherence of the received THz pulses are leveraged to provide an effective approach to suppress grating lobes in the final image. Best performance occurs when the interference factor (IF) and coherence factor (CF) are used together. Our approach can also be tailored to ultrawideband arrays operating in the frequency domain, so long as the overall system bandwidth is comparable to that of a single-cycle pulse. Since densely populated 2-D arrays of photoconductive THz transmitters and receivers are impractical, our sparse array adaptive reconstruction technique can significantly benefit THz imaging applications requiring a large field of view.

Future work includes demonstrating 3-D imaging with sparse arrays, and pushing the limits of array sparseness. The adaptive image reconstruction technique makes possible the development of large 2-D sparse THz arrays for imaging over a wide field of view.

REFERENCES

[1] Chan, W.L., Deibel, J. and Mittleman D.M., "Imaging with terahertz radiation," Rep. Prog. Phys. 70, 1325-1379 (2007).

[2] O'Hara, J. and Grischkowsky, D., "Quasi-optic synthetic phased-array terahertz imaging," J. Opt. Soc. Am. B 21, 1178-1191 (2004).

[3] Federici, J.F., Schulkin, B., Huang, F., Gary, D., Barat, R., Oliveira, F., and Zimdars, D.,"THz imaging and sensing for security applications – explosives, weapons, and drugs," Semicond. Sci. Technol. 20, S266-S280 (2005).

[4] Zhong, H., Redo-Sanchez, A. and Zhang, X.-C. "Identification and classification of chemicals using terahertz reflective spectroscopic focal-plane imaging system," Opt. Express 14, 9130-9141 (2006).

[5] Buma, T. and Norris, T.B. "Time reversal three-dimensional imaging using single-cycle terahertz pulses," Appl. Phys. Lett. 84, 2196-2198 (2004).

[6] Schwartz, J.L., and Steinberg, B.D., "Ultrasparse,ultrawideband arrays," IEEE Trans. Ultrason. Ferroelectr. Freq. Contr.,Vol. 45,376-393 (1998).

[7] John F Federici et al., "THz imaging and sensing for security applications— explosives, weapons and drugs," Semicond. Sci. Technol. 20 S266 (2005).

[8] Daniel M. Mittleman , Rune H. Jacobsen , Martin C. Nuss, "T-Ray Imaging," IEEE J. Sel. Top. Quantum Electron (1996)

[9] M.-L. Li, W. J. Guan, and P.-C. Li, "Improved synthetic aperture focusing technique with applications in high-frequency ultrasound imaging," IEEE Trans. Ultrason. Ferroelectr. Freq. Control, vol. 51, 63-70 (2004).

[10] C. H. Frazier and W. R. O'Brien, "Synthetic aperture techniques with a virtual source element," IEEE Trans. Ultrason. Ferroelectr. Freq. Control 45(1), 196–207 (1998).

[11] P.-C. Li and M.-L. Li, "Adaptive imaging using the generalized coherence factor," IEEE Trans. Ultrason. Ferroelectr. Freq. Control 50(2), 128–141 (2003).

[12] K. W. Hollman, K. W. Rigby, and M. O'Donnell, "Coherence factor of speckle from a multi-row probe," in Proceedings of the 1999 IEEE Ultrasonics Symposium (IEEE, 1999), pp. 1257–1260.

[13] R. Mallart and M. Fink, "Adaptive focusing in scattering media through sound-speed inhomogeneities: The van Cittert Zernike approach and focusing criterion," J. Acoust. Soc. Am. 96(6), 3721–3732 (1994).

[14] M. K. Jeong, "A Fourier transform-based sidelobe reduction method in ultrasound imaging," IEEE Trans. Ultrason. Ferroelectr. Freq. Control 47(3), 759–763 (2000).

[15] M.-L. Li, H. E. Zhang, K. Maslov, G. Stoica, and L. V. Wang, "Improved in vivo photoacoustic microscopy based on a virtual-detector concept," Opt. Lett. 31(4), 474–476 (2006).

[16] D.H. Johnson and D.E. Dudgeon, Array Signal Processing (Prentice Hall, 1993).

[17] J. L. Schwartz, and B.D. Steinberg, "Ultrasparse, ultrawideband arrays," IEEE Trans. Ultrason. Ferroelectr. Freq. Contr. 45, 376-393 (1998).

[18] Q. Wang, R. Wu, M. Xing, and Z. Bao, "A new algorithm for sparse aperture interpolation," IEEE Geos. Rem. Sens. Lett. 4, 480-484 (2007).

[19] A. Austeng and S. Holm, "Sparse 2-D arrays for 3-D phased array imaging – Design methods," IEEE Trans. Ultrason. Ferroelectr. Freq. Contr. 49, 1073-1086 (2002).

[20] J. W. Goodman, Statistical Optics (Wiley-Interscience, 1985).

[21] Z. Zhang and T. Buma, "Adaptive terahertz imaging using a virtual transceiver and coherence weighting," Opt. Express 17, 17812-17817 (2009).